RESEARCH ARTICLE

Hemodynamic Patterning of the Avian Atrioventricular Valve

Huseyin C. Yalcin,[1,2] Akshay Shekhar,[1] Tim C. McQuinn,[3] and Jonathan T. Butcher[1]*

In this study, we develop an innovative approach to rigorously quantify the evolving hemodynamic environment of the atrioventricular (AV) canal of avian embryos. Ultrasound generated velocity profiles were imported into Micro-Computed Tomography generated anatomically precise cardiac geometries between Hamburger-Hamilton (HH) stages 17 and 30. Computational fluid dynamic simulations were then conducted and iterated until results mimicked in vivo observations. Blood flow in tubular hearts (HH17) was laminar with parallel streamlines, but strong vortices developed simultaneous with expansion of the cushions and septal walls. For all investigated stages, highest wall shear stresses (WSS) are localized to AV canal valve–forming regions. Peak WSS increased from 19.34 dynes/cm^2 at HH17 to 287.18 dynes/cm^2 at HH30, but spatiotemporally averaged WSS became 3.62 dynes/cm^2 for HH17 to 9.11 dynes/cm^2 for HH30. Hemodynamic changes often preceded and correlated with morphological changes. These results establish a quantitative baseline supporting future hemodynamic analyses and interpretations. *Developmental Dynamics 240:23–35, 2011.* © 2010 Wiley-Liss, Inc.

Key words: computational modeling; shear stress; blood flow; rheology; mechanotransduction; morphogenesis; mitral valve; embryo; mechanobiology; finite element; simulation; vortex

INTRODUCTION

The formation of the embryonic heart is one of the most fascinating and complex developmental events. Over 100 years of research has documented its changing three-dimensional shape and contraction patterns, although our understanding of the process remains largely qualitative. The vertebrate heart originates as bilaterally symmetric mesodermal fields that fuse to form a tubular structure with the inflow segment caudal to the outflow. This tube then loops and bulges such that the primitive ventricular segment forms caudally to the atrial segment. For higher order vertebrates such as birds and mammals, the myocardial wall of the tube expands, becoming trabeculated, and a septal ridge progresses cranially until it meets with a similar mesenchymal protrusion that divides the atria and ventricles into left and right portions. Concomitant with this process is the formation of the valvular apparatus, which originates as endocardium lining the atrioventricular (AV) canal and outflow tract (Cruz and Markward, 1998). A subset of these cells is induced to transform into mesenchymal cells (called endocardial to mesenchymal transformation, EMT) that invade the underlying gelatinous matrix, remodeling it into cushions that perform valve-like function. These cushions eventually fuse together medially, forming left and right inlets. EMT occurs at Hamburger-Hamilton (HH) stage 16 and cushion fusion approximately 60 hr later at HH26. At this time, a second lateral set of cushions form, eventually remodeling into the lateral leaflets of the AV valve (although in the chick the right AV becomes a muscular flap structure). The residual medial cushion components and the lateral cushions then

become remodeled into thin fibrous leaflets populated by largely fibroblastic phenotypes and quiescent endothelium (Combs and Yutzey, 2009). Recent studies have given significant clarity to the morphogenic phases of the remodeling AV valves as a dynamic three-dimensional event (Butcher and Markwald, 2007). The mechanisms driving these morphogenic processes, however, remain incompletely understood.

The heart continually pumps blood while growing and remodeling, which suggests that hemodynamic stresses within the heart may provide morphogenic cues to guide downstream development (Hove et al., 2003; Forouhar et al., 2006; Culver and Dickinson, 2010). This idea has been studied for at least the past 60 years through largely qualitative means (Patten et al., 1948; Savard et al., 1960; Jaffee, 1965). Early observations of blood flow through the embryonic outflow tract via dye injections suggest that preferred streamlines form prior to its septation into pulmonary and aortic branches (Jaffee, 1965; Yoshida et al., 1983). Changes in these streamlines through mechanical perturbations to cardiac inflow were suggested to precede morphogenetic defects (Hogers et al., 1995; Hu et al., 2009). Groenendijk et al. recently provided mechanistic insight by showing that these inflow hemodynamic alterations caused local endocardial gene expression changes, but correlation with local hemodynamic indices was not carried out (Groenendijk et al., 2005). Reckova et al. showed that ligation of the left atria or banding of the outflow tract alters ventricular myocardial and conduction system maturation, but hemodynamics was not quantified (Reckova et al., 2003). More recently, it was shown that hemodynamics drives valve morphogenesis and function (Vermot et al., 2009), which could be related directly to changes in tissue biological composition (Butcher et al., 2007a). Studies in zebrafish embryos using spherical beads to impede cardiac inflow or outflow also confirm these observations (Hove et al., 2003).

In order to better understand the relationships between mechanical and biological signaling in embryonic development, detailed quantification of the local mechanical conditions is required. Several studies have quantified local myocardial wall strains (Taber et al., 1993; Miller et al., 1997), but quantifying hemodynamics has been more limited. The major techniques have been video-microscopy of dye injections (Hogers et al., 1995; Hu et al., 2009), Doppler ultrasound (Butcher et al., 2007a; McQuinn et al., 2007), and particle-image velocimetry (PIV) (Vennemann et al., 2006). Pulsed dye injections follow blood well but require extremely fast cameras to avoid noise. Doppler ultrasound probes can record blood velocity at much faster rates (>10 kHz), and have been used extensively to quantify global hemodynamic indices in embryonic chick and mouse (Clark and Hu, 1982; Hu and Clark, 1989; Phoon et al., 2004). Doppler ultrasound without B-mode guidance is difficult to accurately place, and is only able to rectify the peak blood velocity without respect to cross-sectional variations (Butcher et al., 2007a). Fast scanning confocal microscopy (Liebling et al., 2006) and optical coherence tomography (Jenkins et al., 2007) have also been used to visualize cardiac morphogenesis and quantify hemodynamics in vivo, but their 3D imaging capacity is limited to very early hearts (pre-HH20).

Many studies have shown that endothelial/endocardial cells are highly sensitive to changes in wall shear stress (WSS) (Girard and Nerem, 1993; Butcher and Nerem, 2006; Butcher et al., 2006; Farcas et al., 2009). Very little, however, is known about the levels and directions of WSS within the developing heart. While relatively straightforward to calculate in straight tubes like blood vessels, the extremely tortuous geometry, small length scales, and changing blood characteristics invalidate many of the simplifying theoretical assumptions commonly applied. Computational fluid dynamics (CFD) modeling is very useful in cardiovascular research for elucidating complex fluid motions where experimental measurement schemes would provide only limited information and/or in cases where key fluidic features are unknown a priori. Previous studies focusing on the adult carotid artery have shown that geometry is the most critical feature for accurate computational analysis (Birchall et al., 2006), which consequently is the most difficult to determine in these small organisms. Few CFD studies on embryonic hearts have been conducted to date. Those that do exist generally apply geometries generated from 3D reconstructions of histological sections (DeGroff et al., 2003; Groenendijk et al., 2005; Liu et al., 2007), which suffer from variable geometry in fixation and processing. We recently adapted micro-computed tomography (Micro-CT) for generating high-resolution images of embryonic heart development, from which we were able to quantify several features of cardiac morphogenesis (Butcher et al., 2007b). This approach was recently used to quantify the hemodynamics within the developing aortic arches (Wang et al., 2009), but to date a comprehensive 3D CFD analysis of intracardiac embryonic heart hemodynamics has not been done. The objective of this study, therefore, was to perform a detailed quantitative analysis of the hemodynamics of the developing left AV region of the embryonic chick heart through the valvulogenic window beginning at EMT (HH17) until onset of condensation of cushion tissue into thin fibrous leaflets (HH30).

RESULTS

In Vivo Diastolic Blood Flow and Rheology in the Left AV Junction

We used high-frequency ultrasound to measure the AV inflow velocities and diameters in embryonic chicks between stages HH17 and HH30, the results of which are shown in Figure 1A–D. We found a monotonic increase in peak AV blood velocity from 2.7 ± 2.194 cm/s to 42.8 ± 1.13 cm/s, similar to other published reports (Butcher et al., 2007a). Peak AV diameter increased from 0.26 ± 0.02 to 0.54 ± 0.03 mm. HH17 and HH23 AV velocity profiles contained two peaks corresponding to the passive and active contraction phases, respectively, confirming our previous results (Butcher et al., 2007a). Only one AV velocity peak was observed in the AV after HH23. Temporal cardiac averaged velocities are 0.89 ± 0.16, 2.13 ± 0.37, 3.08 ± 0.99, 3.85 ± 0.50 cm/s for stages HH17, HH23, HH27, and HH30, respectively.
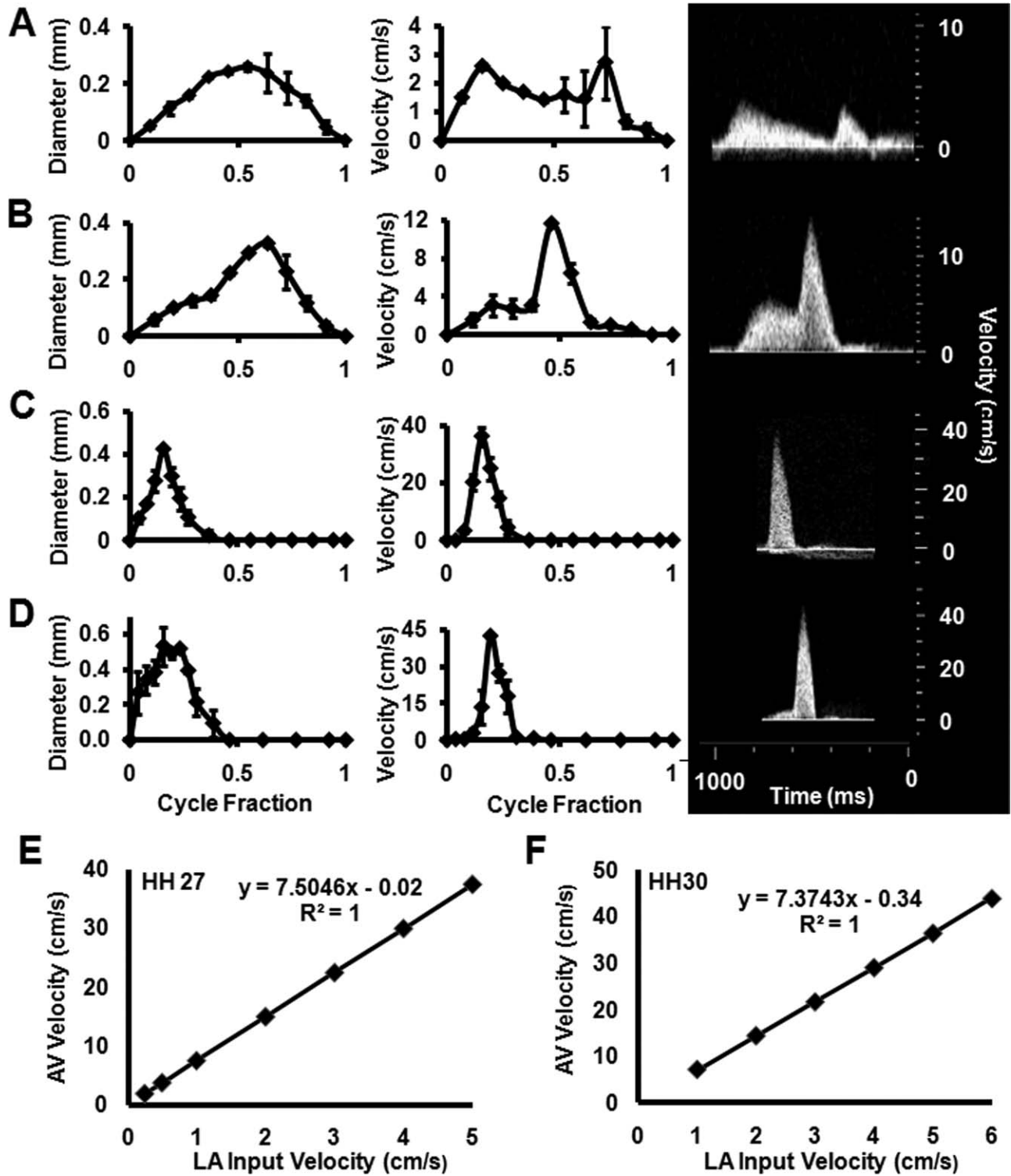
Developmental Dynamics

Fig. 1. Stage-specific AV orifice diameter (left) and peak velocity (right) as measured by ultrasound. Insets on right are representative original Doppler velocity recordings. **A:** HH17. **B:** HH23. **C:** HH 27. **D:** HH 30. Correlation of AV canal velocity with left atrial (LA) input velocity for stages (**E**) HH27 and (**F**) HH30.
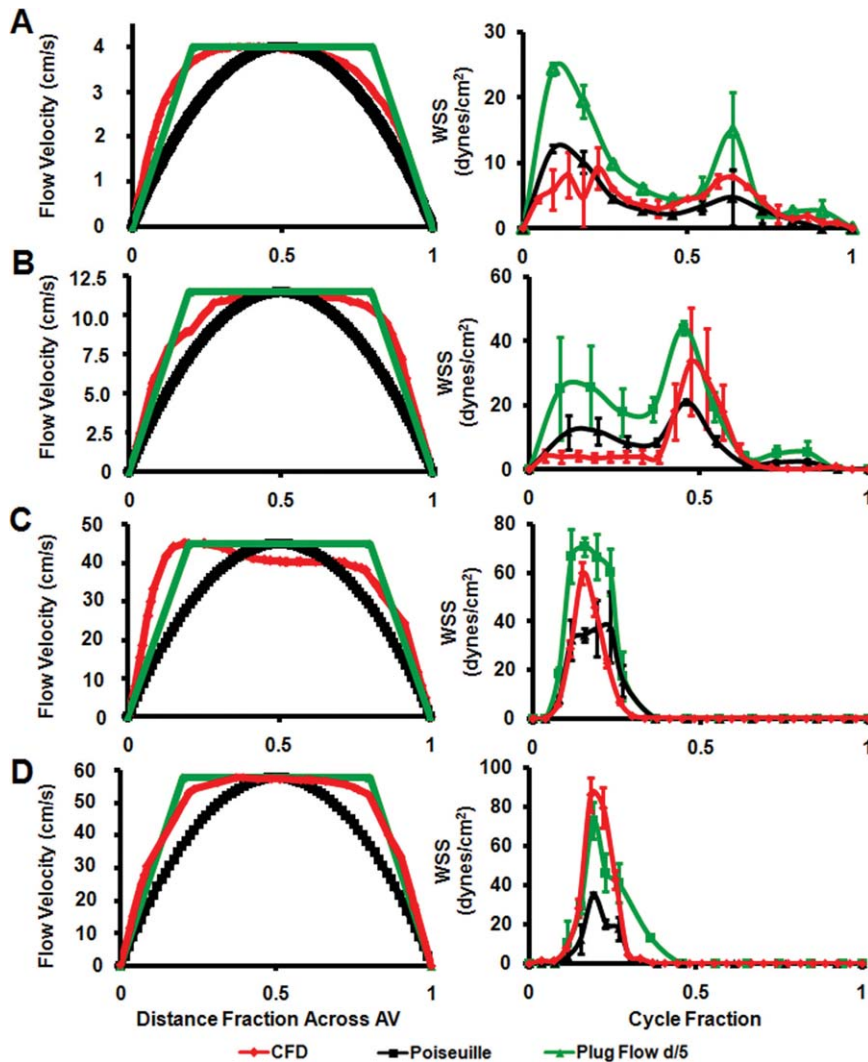
Fig. 2. Stage-specific AV orifice flow profiles at peak velocity (left) and spatially averaged WSS throughout the cardiac cycle (right) as calculated by CFD and from ultrasound with Poiseuille and Plug Flow (boundary layer 1/5th of the diameter) assumptions. **A:** HH17. **B:** HH23. **C:** HH 27. **D:** HH 30.

Generation of Anatomical Geometries and Atrial Inflow Boundary Conditions for CFD Simulations

For these studies, we generated 3D anatomical geometries of the AV canal region and included the adjoining atrial and ventricular segments. Microfil polymer casting enabled us to maintain consistent, physiologically dilated chamber dimensions that were converted to digital volumes via Micro-CT. These static anatomic geometries were used to approximate the "instant" of diastolic inflow. CFD simulations were then conducted to quantify the 3D hemodynamic environment of this entire AV region, including the

partial atrial inflow and ventricular zones. Simulations required static inflow and outflow zones, which we approximated as flat elliptical regions on the partial atrial and ventricular regions. In this way, flow would progress from atrium to ventricle directly. Atrial flow was not possible to measure via Doppler ultrasound because of high noise and directional changes within the contracting chamber, but midline AV Doppler recordings were easily achieved. Since our CFD simulations require this input atrial velocity profile as a boundary condition, we chose to iterate CFD simulations modulating the magnitude of a "fictitious" atrial inflow profile. Correlation curves were established with steady-

flow simulations until CFD simulated midline AV velocity converged with in vivo measurements. This in vivo validated atrial scaling factor was then applied to the AV midline velocity profile and used as the input for CFD simulations. For HH17 and HH23, back calculated atrial velocities were found to be very close to measured in vivo AV velocities (i.e., scaling factor around 1). Therefore, in simulations, measured velocities were used directly for these stages. For HH27 and HH30, however, scaling factors were 7.50 and 7.37, respectively (Fig. 1E and F).

Boundary Layer Estimation

At peak velocity, flow profiles in the mid channel surfaces (i.e., for HH17, line connecting the mid inner curvature and mid outer curvature; for HH23, line connecting the mid ventral cushion and mid dorsal cushion; and for HH27 and HH30, line connecting the mid septal cushion and mid mural cushion; see Fig. 9 for cushion regions) were plotted in order to see flow characteristics (Fig. 2, left column). At HH17, velocity profile resembled Poiseuille Flow distribution whereas in other stages it resembled Plug Flow with boundary layer thickness around 1/5th of the diameter. CFD WSS values averaged spatially for all traced regions (shown in Fig. 9), were compared with WSS values calculated with Plug Flow and Poiseuille Flow assumptions (Fig. 2, right column). Similarly, HH17 CFD WSS results throughout cardiac cycle are closer to Poiseuille Flow results than Plug flow whereas in other stages this resemblance is reversed.

Pressure Drop Validation

We next compared CFD simulated pressure drop through the AV canal with calculated pressure drop from ultrasound measured velocities (Equation 3 in Experimental Methods section) as well as direct measurements (Hu and Clark, 1989) (Fig. 3). At HH17, CFD pressure drop at peak velocity and pressure drop calculated from Doppler measured peak velocities are 0.014 ± 0.004 and 0.0029 ± 0.0005 mmHg and both of these values are significantly lower than direct measurement, which is $0.32 \pm$ mmHg.

At HH23, CFD result compares well with direct measurement, 0.38 ± 0.11 versus 0.40 ± 0.03 mmHg whereas Doppler velocity pressure calculation resulted in significantly lower value, 0.05 ± 0.004 mmHg. At HH27, CFD result and Doppler velocity pressure calculation are not significantly different, 0.61 ± 0.027 versus 0.50 ± 0.014 mmHg ($P > 0.05$) and these values compare well with direct measurement 0.56 ± 0.03. Similarly at HH30, CFD result and Doppler velocity pressure calculation are not significantly different, 0.71 ± 0.024 versus 0.69 ± 0.036 mmHg ($P > 0.05$) and these values compare well with direct measurement, 0.82 ± 0.03 mmHg. Taken together with the boundary layer analysis, these results demonstrate that our static wall geometries and inflow approximations of the in vivo state are reasonable.

CFD Simulation Results

Peak WSS increased monotonically from 19.34 ± 4.45 at HH17 to 287.18 ± 67.45 dynes/cm^2 at HH30 (Table 1). Similarly, spatially averaged WSS at peak velocity increased monotonically from 9.17 ± 3.2 to 86.27 ± 8.6 during development. Spatially and temporally averaged stress varied between 3.62 ± 0.32 and 9.11 ± 1.06. Peak Reynolds numbers for all cases were between 0.81 ± 0.01 and 10.6 ± 0.59. Peak Womersley numbers were less than 1. Peak vorticity increased monotonically from 2,576.11 ± 283.79 at HH17 to 20,679.6 ± 4,579.13 1/s at HH30. Pressure drop through the AV canal increased from 0.014 ± 0.004 to 0.71 ± 0.024 mmHg.

HH17 Simulations

At this stage, the embryonic heart resembled a looped tube with an atrial bulge not yet containing defined left and right segments. CFD simulations determined that velocity streamlines were essentially parallel through the AV canal during the entire cardiac cycle, demonstrating unidirectional laminar flow (Fig. 4A). Spatially averaged WSS on the inner curvature was compared with that of the outer curvature throughout cardiac cycle (Fig. 4B, see Fig. 9 for traced regions). Simulations determined a peak WSS of 13.4 ± 3.74 dynes/cm^2 on inner curvature and 7.76 ± 3.17 dynes/cm^2 on outer curva-

ture. Both of these peak stresses occurred at peak velocity.

HH23 Simulations

At HH23, the AV canal is now rotated 90° to the right such that the cushions are now in a ventral/dorsal configuration. The left and right atrial cavities are now well formed but not septated and the AV cushions protrude significantly into the canal, creating a "dog-bone"-like lumen shape when viewed from the atria. In addition, the primitive left and right ventricular segments have expanded into respective cavities. Endocardial trabeculations have formed and the interventricular septum has begun to advance cranially through the heart. The ventricular cavities expand below the AV cushions creating sinus-like spaces. Ultrasound measurements and CFD simulations show that blood flow diverges away from the midline of the canal and concentrates through the larger "head" regions on the right and left sides (Fig. 5A). Pulsatile flow simulations show the early inflow velocity streams in HH23 hearts are laminar. During this diastolic filling phase, blood flow is diverted heterogeneously into the left and right ventricular segments. Simulations showed that proportions of blood from the left and right atria were delivered to the ventricular segment of the opposite side. This phenomenon was dependent on the phase of the cardiac cycle. During passive filling (P wave), proportions of blood from the left atrial segment were diverted into the right ventricular segment, but in active filling (A wave) this trend was reversed (right into left). Shortly after peak inflow velocity is reached, vortices develop in the sinus cavities about axes perpendicular to the inflow direction. The locations of
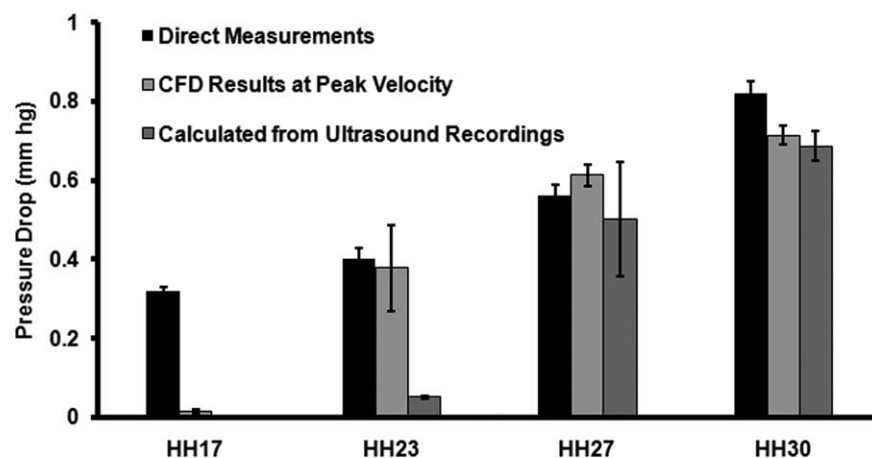

Fig. 3.   Change in pressure across the AV canal region.

TABLE 1. CFD Simulation Results[a]

Stage (HH)	Peak WSS, (Dynes/cm^2)	Spatially Averaged WSS at Peak Velocity (Dynes/cm^2)	Spatially and Temporally Averaged WSS (Dynes/cm^2)	Peak Reynolds Number	Peak Womersley Number	Peak Vorticity (1/s)	Peak Dp (mmHg)
17	19.34 (4.45)	9.17 (3.2)	3.62 (0.32)	0.81 (0.01)	0.23 (0.005)	2576.11 (283.79)	0.014 (0.004)
23	78.33 (37.09)	33.59 (16.84)	6.79 (3.22)	10.60 (0.59)	0.34 (0.001)	9737.44 (2911.19)	0.38 (0.21)
27	250.09 (51.49)	59.7 (4.6)	6.1 (0.52)	7.74 (0.37)	0.42 (0.008)	18171.84 (4034.86)	0.61 (0.027)
30	287.18 (67.45)	86.27 (8.6)	9.11 (1.061)	10.42 (0.78)	0.41 (0.008)	20679.6 (4579.13)	0.71 (0.024)

[a]Values in parentheses are standard deviations.
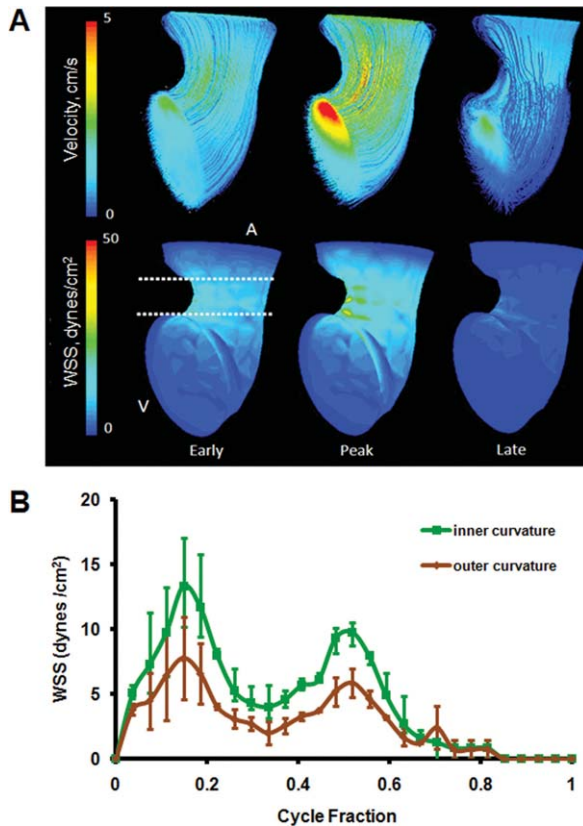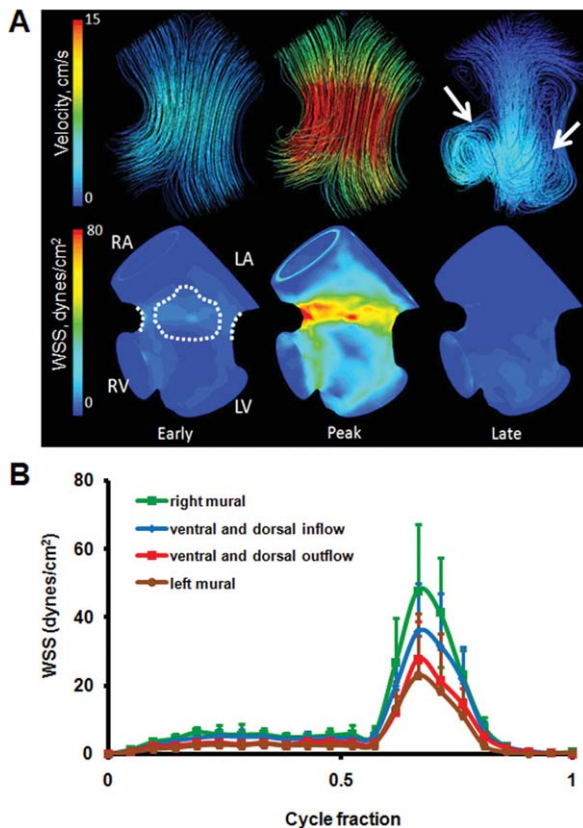
Developmental Dynamics

Fig. 4.

Fig. 5.

these vortices correlate with the morphogenesis of the outflow (ventricularis) surface of the AV cushions (shown with arrows on Fig. 5A). At HH23, the retrograde flow in these vortices appears to create a downward (towards the ventricle) pointing lip in these cushions, which becomes more pronounced as development advances. These vortices persist throughout the remainder of the cardiac cycle. Spatially averaged WSS on the right and left mural surfaces and ventral and dorsal midlines were compared throughout the cardiac cycle (Fig. 5B; see Fig. 9 for traced regions). Values for ventral and dorsal inflow were not significantly different and, therefore, averaged and plotted together. Similarly, ventral and dorsal outflow values are plotted together. CFD simulations determined that the peak WSS exists on the right mural surface (47.74 dynes/cm^2), or where the muscular flap valve will develop. At this stage, however, there are no cushion masses present. For the left mural surface, peak WSS value was 23.12 dynes/cm^2. Similarly, for ventral/dorsal inflow surfaces, peak value was 35.75 dynes/cm^2 and for ventral/dorsal outflow 27.78 dynes/cm^2. Peak stresses occurred at peak velocity.

HH27 Simulations

At this stage, the two cushions have fused together. While the central region of this mass forms a fibrous septum that joins with the dorsal mesenchymal protrusion and the ventricular septum, the lateral edges become remodeled into valves. From 3D Micro-CT, the septal cushion extended around the inlet orifice from about 7 o'clock on an anterior-posterior axis to about 2 o'clock. The septal
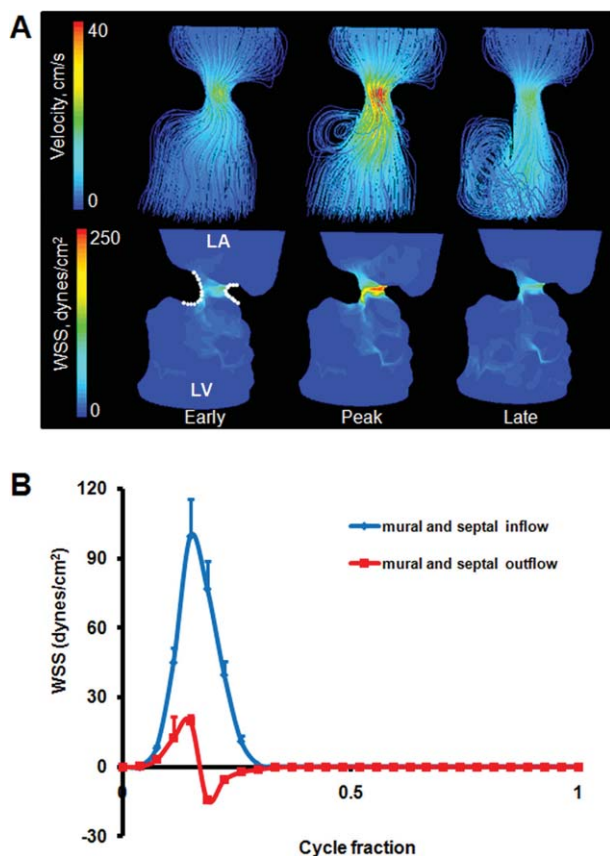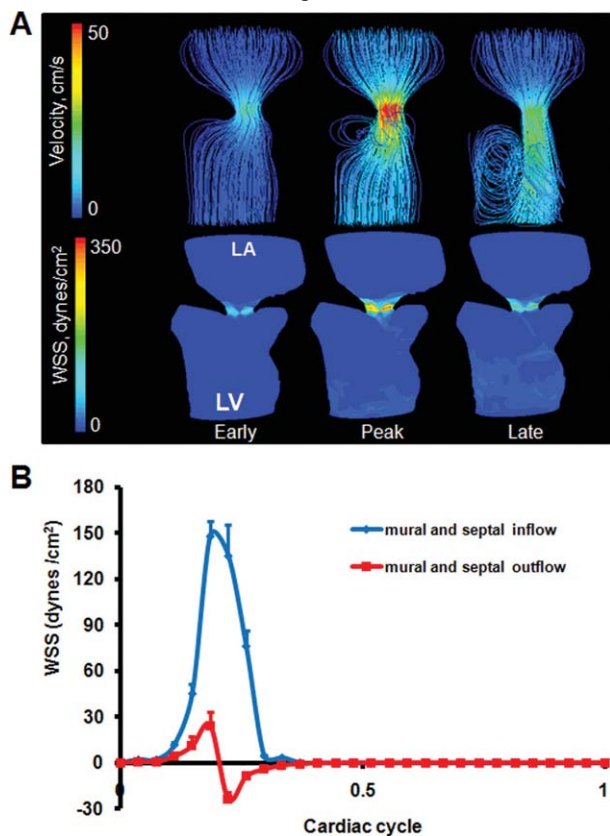
Developmental Dynamics

Fig. 6.

Fig. 7.

cushion overlaid the upper left ventricle whereas the left mural cushion occupied the remainder of the annulus. The septal cushion was approximately three times larger than the mural cushion. CFD simulations showed a strong jet through the AV inlet, causing high shear stresses on the inflow cushion surfaces with flow separation from the outflow surface and myocardial walls (Fig. 6A). The cushions are shaped so that this jet is slightly "C" shaped, and impacts the free wall of the left ventricle with a large degree of vorticity. The blood rebounds off this wall and spirals back towards the inlet. Flow in the opposite direction as the original injection bolus is, thus, experienced by the cushion surfaces facing the ventricle (represented as negative numbers). Spatially averaged WSS on the septal and mural cushion surfaces were compared throughout the cardiac cycle (Fig. 6B; see Fig. 9 for traced regions). Values for septal and mural inflow as well as septal and mural outflow were not significantly different, therefore averaged and plotted together. We found peak WSS of 99.62 dynes/cm^2 on the inflow surface, and 19.62 dynes/cm^2 on the outflow. Peak shear stresses occurred at peak inflow velocity. After peak velocity, spiraling flow occurs at the outflow surfaces of the cushions and persists throughout the rest of the cardiac cycle. This results in a "negative" shear stress that is opposite the original inflow direction.

HH30 Simulations

The AV cushions have condensed significantly but not completely, closer to resembling leaflets. The "C" shape and downward pointing of the free edge of the septal leaflet was more pronounced. The left ventricular

Fig. 6. **A:** 3D hemodynamic environment in the AV region, Stage HH 27. **B:** Spatially averaged WSS on the inflow and outflow surfaces throughout cardiac cycle. LA, left atria; LV, left ventricle.

Fig. 7. **A:** 3D hemodynamic environment in the AV region, Stage HH 30. **B:** Spatially averaged WSS on the inflow and outflow surfaces throughout cardiac cycle. LA, left atria; LV, left ventricle.

outlet is now contiguous with the left ventricle, extending from underneath the septal/anterior leaflet. Unlike previous stages where the ventricle lumen shape was wider at the bottom, the ventricle at HH30 was wider at the top, which is typical of the mature shape. The orifice area between the leaflets was significantly larger than at HH27, but the inflow velocity was also much greater. The more pronounced "C" shape of the septal leaflet at this stage created a similarly shaped jet of blood during the active phase of inflow that strikes the left free wall of the left ventricle (Fig. 7A). This again caused blood to spiral back towards the top of the ventricle. Spatially averaged shear stresses on the septal and mural cushions were compared throughout the cardiac cycle (Fig. 7B; see Fig. 9 for traced regions). We found peak WSS 148.25 dynes/cm^2 on the inflow surface, and 24.3 dynes/cm^2 on the outflow, which are both higher than values at HH27. Peak stresses occurred at peak velocity. After peak velocity, spiraling flow along the outflow surface of the cushions results in a "negative" shear stress with respect to the inflow direction. This flow pattern persists throughout the rest of the cardiac cycle.

DISCUSSION

Hemodynamics is an important epigenetic factor driving cardiogenesis and alterations in normal blood flow are postulated as a major source for congenital heart defects (CHD). Many CHD arise relatively late in cardiogenesis, predominantly through malformation of the valvuloseptal structures (Combs and Yutzey, 2009). Fetal cardiac intervention in utero has the potential to alleviate altered hemodynamic signaling to potentially rescue serious defects at birth (Kohl, 2002; Tworetzky et al., 2004). Recent studies have suggested that embryonic endocardial and endothelial phenotype is sensitive to hemodynamic changes in vivo (Groenendijk et al., 2005; Vermot et al., 2009), but without a rigorous quantification of local changes in mechanobiologically relevant hemodynamic indices (e.g., wall shear stress) our ability to translate these observations into deeper understanding and clinical therapies remains limited.

Direct measurement of shear stress inside extremely small, rapidly moving embryonic hearts is currently impossible for much of cardiac development. CFD simulation is a powerful alternative strategy to estimate local hemodynamic parameters and predict their changes to altered loads, but necessitate anatomically accurate geometries, physiological blood rheology, and dynamic flow boundary conditions. Before the current study, simulations were conducted on either simplified 2D wall geometries (Biechler et al., 2010) or reconstructions from thin sections and animal hearts (DeGroff et al., 2003; Groenendijk et al., 2005; Liu et al., 2007). These approaches lack the ability to render complex tortuous anatomy often present in the embryonic valve regions, and as a result the hemodynamic predictions in critically important locations can be far different from the native state. More direct analysis of shear stress in early embryonic hearts is possible via obtaining flow profiles with PIV techniques (Vennemann et al., 2006). Flow and stress fields were quantified in the outflow tract of an HH17 embryo in a recent study (Poelma et al., 2010). However, optical inaccessibility prevents extension of this technique to older embryos. We pioneered the use of Micro-CT to create high-resolution ($\sim$10 μm) anatomical 3D geometries in chick (Butcher et al., 2007b). This technique was recently adapted in a CFD study on aortic arch morphogenesis of chick embryos (Wang et al., 2009) and was also used in the current study. Similar to these prior CFD simulation studies, we approximated the ventricular inflow (diastolic) phase of the cardiac cycle with static (non-moving) wall geometry. Blood velocity is near zero for almost all of the cardiac cycle outside of the initial inflow jet, which we determined was simultaneous with minimal change in AV lumen diameter, together suggesting moving boundaries are not a major factor for this case. In general, anatomical CFD simulations create a conservative upper bound of the true hemodynamic flow because "solid" walls and no-slip boundaries that tend to increase wall shear stresses don't exist naturally. More advanced Fluid-Structure Interaction (FSI) simulation would be able to han-

dle more complexity, but requires detailed quantification of the wall geometry and local tissue mechanics. New techniques are coming online to enable these pursuits (Degenhardt et al., 2010; Butcher et al., 2007b), but to date these dynamic features have not been measured. In this study, however, we rigorously iterated our simulations with respect to direct in vivo flow measurements, which resulted in closely matching solutions where comparable that justify these approximations.

Viscosity is an important parameter for CFD models on blood flow. For early stages of development (before HH17 for chick embryos), effect of red blood cells on viscosity is negligible and blood can be accepted as Newtonian. For later stages, however, viscosity will depend on the shear rate and blood needs to be taken as Non-Newtonian (Hierck et al., 2008). In the current study, Non-Newtonian blood flow assumption is incorporated by formulating the blood flow viscosity with shear rate (Fig. 8) based on previous studies on avian blood viscosity (Rychter et al., 1955; Usami et al., 1970). Peak Reynolds Numbers for all the stages were less than 11 (Table 1), which confirms laminar flow with significant contribution of viscous effects (Stokes behavior). Peak Womersley Numbers were less than 1.

A critically important and often neglected final step in biological CFD simulations is to validate model predictions with measured data. In this study, we compared CFD WSS values with values calculated from direct in vivo flow measurements. We compared the standard Poiseuille flow assumption with various Plug Flow boundary layer approximations (Fig. 2). For all the analyzed stages, CFD simulated results are quantitatively similar to more directly calculated stresses. At HH17, simulation results are closer to Poiseuille values whereas in other stages they are closer to Plug Flow values. AV orifice flow profile at HH17 resembled the parabolic Poiseuille profile (consistent with Newtonian behavior) whereas in later stages the profile resembled Plug Flow profiles. We also compared pressure drops in AV canal from simulations with direct measurements and values calculated from ultrasound-generated velocities
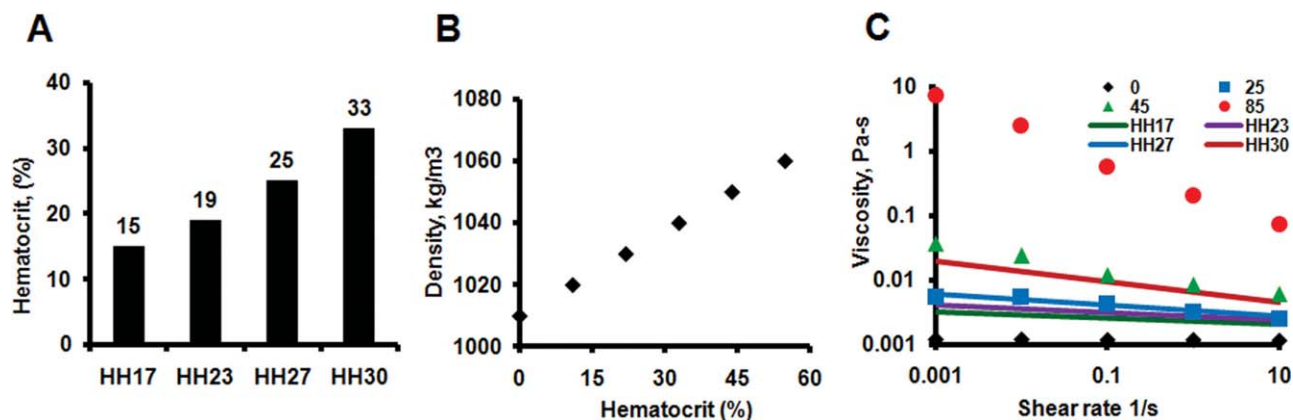
Fig. 8. Stage-dependent blood rheology. **A:** Hematocrit amounts for stages (adapted from Rychter et al., 1955). **B:** Hematocrit-dependent blood density (adapted from Usami et al., 1970). **C:** Nonlinear power law relationship for shear rate–dependent viscosity. Dots represent correlations generated based on hematocrit amounts and lines are based on embryonic stages.
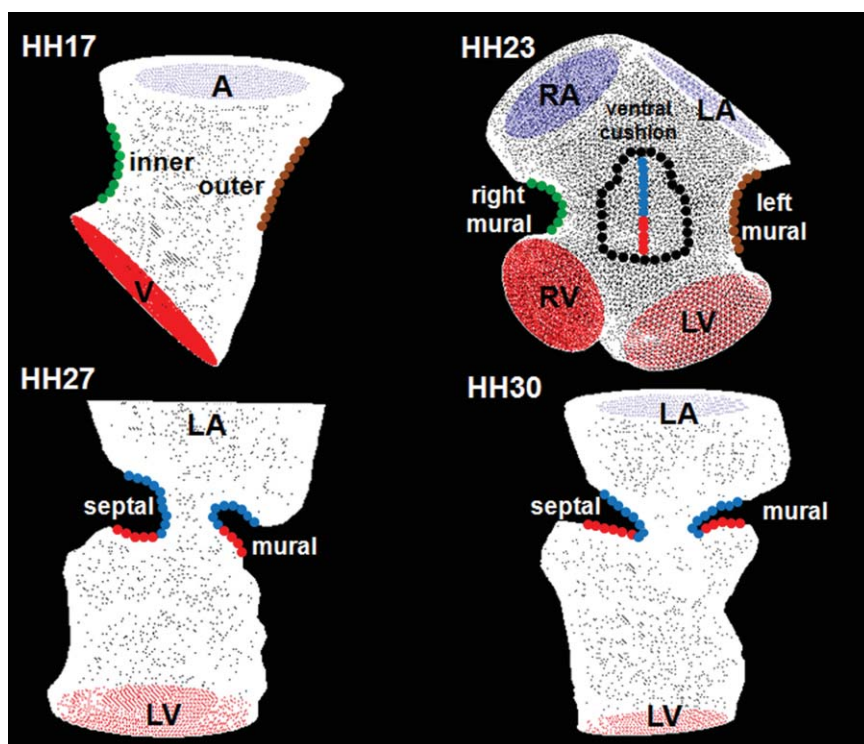

Fig. 9. Cushion regions where the WSS were traced (shown with dotted lines). Inflow segments are blue, outflow are red for separated regions. Trace colors match with plot colors for regions in Figures 4–7. At HH24, dorsal cushion is on the other side of the geometry. A, atria; V, ventricle; L, left; R, right.

result is consistent with previous studies (Hierck et al., 2008). The inner and outer curvature zones are important morphogenetic regions, the inner for cardiac jelly expansion and cushion remodeling, while the outer is for ventricular trabeculation. These results suggest that low wall shear stress may help promote regression of cardiac jelly and the formation of myocardial trabeculations. Higher wall shear stress, on the other hand, may promote cardiac jelly expansion and EMT. A mechanistic link between hemodynamics and EMT so far has been difficult to test experimentally. The excised avian embryonic heart can loop without blood flow (Manning and McLachlan, 1990), and we have observed in similar experiments invaded mesenchyme in the AV and outflow valvulogenic regions (J.T. Butcher, unpublished results). Recent studies in zebrafish show that reversing flows through temperature or heart rate modification promote endocardial ring formation and invagination, while embryo culture with doses of myocardial toxins inhibit (Vermot et al., 2009). Mechanistic understanding will require in vitro experimentation where hemodynamic parameters can be isolated from myocardial signaling. While outside the scope of this study, our data provides a quantitative foundation for these experiments.

AV cushion expansion at HH23 results in both elevated inflow endocardial surface shear stress and recirculating flow inferior to the cushions (Fig. 5). Shear stresses on the ventricular walls are now significantly less

(Fig. 3). All 3 values compare well for later stages but not for earlier stages. One potential explanation for the discrepancy at HH17 may be that an elevated hydrostatic pressure exists from interstitial tissue motions and flows (Forouhar et al., 2006; Butcher et al., 2007a), but this is very challenging to independently calculate and experimentally decouple. Nevertheless, we believe this innovative combination of anatomically precise wall geometries, stage-dependent blood rheology, and iterative feedback with in vivo measurement create the best representation of physiological embryonic AV hemodynamics to date.

Our results show that for HH17 flow is unidirectional and laminar and the inner curvature is exposed to larger stresses than outer curvature throughout the cycle (Fig. 4). This

than the cushion surface. Interestingly, the right mural cushion surface is exposed to the highest stresses and the left mural surface the lowest. Since the right side becomes a muscular flap valve while the left remodels into a fibrous leaflet, these results suggest shear stress thresholds may precede and in part specify this change. Interestingly, Sedmera et al. using a left atrial ligation (LAL) model showed that restricting inflow creates thickened, poorly remodeled cushions in both the left and right AV valves, while conotruncal banding (CTB) produced hypercontracted left AV valves (Sedmera et al., 1999). Our results suggest that LAL would reduce AV shear stress on the left side and increase on the right side, while CTB would increase wall shear stress on both sides of the AV canal. Furthermore, alterations in preload and/or afterload hemodynamics will give different shear stress profiles difficult to predict a priori, though they can be easily simulated computationally. Well-controlled in vitro experimental systems that can isolate and test individual hemodynamic parameters on embryonic heart explants will be required to prove causality (Goodwin et al., 2005; Butcher and Nerem, 2006). The spiraling vortex zones initiated at HH23 and persisting through HH30 precede, and magnitudes correlate with, ventricular lumen expansion, which suggests that this hemodynamic index may independently regulate this morphogenic process. The inflow surface of the AV cushion is consistently exposed to significantly higher shear stress than the outflow surface from HH23 to HH30, and the flow patterns are consistent but different. They suggest that high unidirectional shear stress may help promote cushion extension in the direction of flow (down into the ventricle), while lower recirculating flows encourage a sculpting process that separates the primitive valve from the junctional myocardium. A similar process was suggested over 25 years ago by Colvee and Hurle (1983) for the outflow cushions, but until this study, had not been quantified for any embryonic valve. Complementing this flow pattern was the "C"-shaped AV orifice shape we identified, which helps promote asymmetric filling of the ventricle. Our simulations suggest

that the ricochet of blood off the free LV wall during diastolic filling helps conserve fluid momentum and cardiac efficiency because the direction of spiraling is such that fluid mass is already moving in the direction it needs to go to reach the outflow tract of the heart. A similar process has been identified in human heart function (Kilner et al., 2000), but this is the first identification and measurement in an embryonic system. The increasing AV canal asymmetry over development reported in this study (HH23–HH30) suggests that this is a previously unrecognized and important aspect of cardiac functional maturation.

In conclusion, this study establishes quantitative 3D mappings of biologically important hemodynamic indices within the developing avian atrioventricular canal. We identify several previously unrecognized correlations between shear stress, vorticity, and cardiac morphogenesis that suggest they may be important guiding factors. It is, therefore, likely that slight alterations in these values could have profound effects on morphogenesis. Similarly, restoring normal hemodynamic signaling may be a promising strategy for rescuing congenital malformations. It will be essential to develop animal model systems that can precisely alter local hemodynamic signaling and complementary in vitro test systems to more fully study these new research directions. Our results establish normal hemodynamic benchmarks that can now be used in bioreactor studies to simulate AV inflow conditions to connect hemodynamic and molecular changes or to drive the maturation of engineered embryonic cardiac tissues.

EXPERIMENTAL PROCEDURES

Microfil Cast Creation

We created casts of embryonic hearts by perfusing Microfil (Flow-Tech, Carver, MA) into microvascular lumens through drawn glass capillary microneedles (Butcher et al., 2007b). In this technique, Microfil solution polymerizes into a cast, preserving the cardiac chambers at physiologically dilated volume condition with open valves.

In Vivo Hemodynamic Measurements

We measured the inflow velocity to the AV canal using B-mode-guided Doppler ultrasound (Vevo770, Visualsonics, Inc., Toronto, Candad). B-mode imaging was also used to simultaneously measure the time varying diameter of the AV canal at the midline of the closure region (Butcher et al., 2007a; McQuinn et al., 2007). Embryos cultured outside their egg shells were used for these measurements. This culture technique is based on incubating embryos for approximately 2.5 days (HH16–17), and cracking eggs into an ex-ovo culture system slightly modified from those previously described (Auerbach et al., 1974; Butcher et al., 2007a; McQuinn et al., 2007). Eggs were aseptically transferred to a polyurethane membrane (Saran Wrap) affixed circumferentially inside a plastic cup partially filled with sterile water. Three-quarters filled 9-oz plastic cups with a top diameter of 8 cm were used. Embryos were cultured outside of the shell for up to 4 additional days (HH30) in a modified portable environmental chamber (1602N Thermal Air, GQF Manufacturing Co, Savannah, GA). The culturing technique can be seen in a video article (Yalcin et al., 2010). Shell-less cultured embryos were transferred to the ultrasound system and a small meniscus of warmed Tyrode's solution provided aqueous contact between the ultrasound probe and the embryo. The probe (30 or 55 MHz) was positioned in 3D space using micromanipulators and clamped at the appropriate angle for imaging. After imaging, the embryos were transferred back to the incubator and allowed to recover. In this fashion, we were able to serially image the embryos for up to 6.5 days.

Blood Rheology

The density and shear thinning behavior of blood are significantly dependent on hematocrit, which varies between stages of embryonic development and invalidates Newtonian flow assumptions. Previous studies have quantified the rheology of avian blood (Usami et al., 1970) and embryonic chick blood (Rychter et al., 1955) cell content, respectively. We used this data to

formulate a Non-Newtonian power law representation of blood viscosity, with the coefficients determined for each stage of interest (Fig. 8). We used the viscosity of water (0.001 Pa-s) as a lower limit and (10 Pa-s) as an upper limit.

Micro-CT Imaging and Reconstruction

Microfil perfused embryonic bodies were dissected away from the vitelline network and placed in 3 ml tubes filled with PBS. The embryos were then scanned via Micro-CT (Scanco, Inc., Wayne, PA) at 10 μm voxel resolution (approximately 400 slices/embryo). An initial scout image was generated at low resolution to confine the high-resolution scan to just the heart region. The datasets were reconstructed into 3D geometry using internal Scanco software and the cardiac anatomy segmented as previously described and exported as STL files (Butcher et al., 2007b). Reconstructions were then down-sampled and smoothed to 5,000 faces using AMIRA, which created a manageable file size (<10 MB) without sacrificing anatomical precision. Files were then converted to IGES using Geomagic (Geomagic, Inc., Research Triangle Park, NC) and imported into GAMBIT (ANSYS Inc., Canonsburg, PA). The atrium, ventricle, and AV canal lumen regions were isolated with the left side chosen for post-septated stages (HH27 onwards). The atrium was virtually sectioned approximately 50% through its height to simulate inflow conditions. The apex region of the ventricle was also sectioned to simulate filling. For HH23, both left and right inlets and outlets were created from the anatomies.

Simulations

The geometries were then meshed using GAMBIT varying both surface and volume grids resulting in densities between 50,000 and 500,000 tetrahedral elements. Meshed AV anatomies were then imported into a CFD solver developed for second-order double precision 3D pressure driven flows using complex subject specific flows (ANSYS 12 FLUENT, ANSYS Inc.). Auxiliary simulations were conducted to determine Mesh-independent solu-

tions, which were obtained with at most 300,000 elements for all stages processed, henceforth all simulations were conducted with 300,000 tetrahedral elements. Pulsatile CFD simulations were then initiated using inlet flow conditions from the Doppler measurements and stage-dependent blood rheology. Between 30 and 50 time steps were used for each simulation and up to 1,000 iterations per time step were utilized. Convergence was enforced by reducing the residual of the continuity equation, as well as x-, y-, and z-momentum to 10^{-6} for all time steps. Simulations were continued through multiple cardiac cycles until solutions were periodic for each time step. Solutions completed in up to 48 hr (earlier stages converged in less than 2 hr) on a dual-core (3 GHz) workstation with 3 GB ram.

In Vivo WSS and Pressure Drop Approximation

Boundary layer flow fields in rapidly moving walls in conditions such as early chick heart are extremely challenging to determine. CFD simulations of AV inflow with non-moving boundaries were compared to in vivo results using Doppler and B-mode generated velocity profiles and dynamic 2D wall geometry, respectively. At each phase of the cardiac cycle, AV canal diameter and blood velocity were obtained at the center of the cushion apposition zone. We then generated WSS approximations using standard Poiseuille Flow assumptions as well as boundary layer models (Plug Flow) (Wilcox, 1997).

For Plug Flow, the following shear stress formula was used;

$$\tau = \mu \frac{du}{dy} \text{(Wilcox, 1997)} \qquad (1)$$

where τ is shear stress, μ is viscosity, and du/dy is differentiation of the axial flow velocity at the wall with respect to the axis pointing channel center. To obtain boundary layer thicknesses, we analyzed the shape of the flow profiles at the mid-valve surface at peak velocity in our CFD simulations and assumed that this profile is not changing throughout the cycle. Non-Newtonian viscosity was applied using the power law generated from the rheology curves (Fig. 8).

For Poiseuille Flow, the following shear stress formula was used;

$$\tau = \frac{4 \cdot \mu \cdot u_m}{d} \text{(Wilcox, 1997)} \qquad (2)$$

Here u_m is the mean flow velocity (from Doppler recordings) and d is the diameter (from B mode recordings). Viscosity here was taken as 0.001 Pa-s.

To calculate pressure difference across the channel, the following formula was used;

$$dP = \frac{\rho}{2}(u_2{}^2 - u_1{}^2) \text{ (DeGroff, 2002)} \qquad (3)$$

where P is pressure, ρ is density, and u is velocity. Here u_2 is the Doppler measured velocity and u_1 is blood velocity downstream, which was assumed to be 0.

Regions to Trace Wall Shear Stress

Figure 9 shows representative geometries where we traced WSS at each time point in the cardiac cycle. At HH17, shear stress was traced in the inner curvature and outer curvature. At HH23, we traced right mural surface, left mural surface, midline of ventral endocardial cushion, and midline of dorsal endocardial cushion. Midlines of endocardial cushions were divided into inflow and outflow segments where outflow region is where the cushion bends back towards the ventricular wall. At HH27 and HH30, we traced left mural and left septal cushion surfaces. These cushions were separated into inflow and outflow segments where inflow surfaces were exposed to jet-like flows and outflow surfaces to circulatory flows.

Endpoints and Statistical Analysis

Morphological changes and blood flow streams were compared qualitatively and quantified where appropriate. Data were summarized in both cycle-averaged and peak values for each stage. Standard deviations were given in reporting results. Hemodynamic variables (WSS, Reynolds Number, Womersley Number, pressure, etc.) for each simulation were compared using Analysis of Variance (ANOVA)

followed by modified *t*-test with $P < 0.05$ denoting significance.

REFERENCES

Auerbach R, Kubai L, Knighton D, Folkman J. 1974. A simple procedure for the long-term cultivation of chicken embryos. Dev Biol 41:391–394.

Biechler SV, Potts JD, Yost MJ, Junor L, Goodwin RL, Weidner JW. 2010. Mathematical modeling of flow-generated forces in an in vitro system of cardiac valve development. Ann Biomed Eng 38:109–117.

Birchall D, Zaman A, Hacker J, Davies G, Mendelow D. 2006. Analysis of haemodynamic disturbance in the atherosclerotic carotid artery using computational fluid dynamics. Eur Radiol 16: 1074–1083.

Butcher JT, Markwald RR. 2007. Valvulogenesis: the moving target. Phil Trans R Soc Lond B Biol Sci 362:1489–1503.

Butcher JT, Nerem RM. 2006. Valvular endothelial cells regulate the phenotype of interstitial cells in co-culture: effects of steady shear stress. Tissue Eng 12: 905–915.

Butcher JT, Tressel S, Johnson T, Turner D, Sorescu G, Jo H, Nerem RM. 2006. Transcriptional profiles of valvular and vascular endothelial cells reveal phenotypic differences: Influence of shear stress. Arterioscler Thromb Vasc Biol 26:69–77.

Butcher JT, McQuinn TC, Sedmera D, Turner D, Markwald RR. 2007a. Transitions in early embryonic atrioventricular valvular function correspond with changes in cushion biomechanics that are predictable by tissue composition. Circ Res 100:1503–1511.

Butcher JT, Sedmera D, Guldberg RE, Markwald RR. 2007b. Quantitative volumetric analysis of cardiac morphogenesis assessed through micro-computed tomography. Dev Dyn 236:802–809.

Clark EB, Hu N. 1982. Developmental hemodynamic changes in the chick embryo from stage 18 to 27. Circ Res 51:810–815.

Colvee E, Hurle JM. 1983. Malformations of the semilunar valves produced in chick embryos by mechanical interference with cardiogenesis. An experimental approach to the role of hemodynamics in valvular development. Anat Embryol (Berl) 168:59–71.

Combs MD, Yutzey KE. 2009. Heart valve development: Regulatory networks in development and disease. Circ Res 105: 408–421.

Cruz MD, Markward R, editors. 1998. Living morphogenesis of the heart. Boston: Birkhäuser.

Culver JC, Dickinson ME. 2010. The effects of hemodynamic force on embryonic development. Microcirculation 17: 164–178.

Degenhardt K, Wright AC, Horng D, Padmanabhan A, Epstein JA. 2010. Rapid 3D phenotyping of cardiovascular development in mouse embryos by micro-CT with iodine staining. Circ Cardiovasc Imag 3:314–322.

DeGroff CG. 2002. Doppler echocardiography. Pediatr Cardiol 23:307–333.

DeGroff CG, Thornburg BL, Pentecost JO, Thornburg KL, Gharib M, Sahn DJ, Baptista A. 2003. Flow in the early embryonic human heart: a numerical study. Pediatr Cardiol 24:375–380.

Farcas MA, Rouleau L, Fraser R, Leask RL. 2009. The development of 3-D, in vitro, endothelial culture models for the study of coronary artery disease. Biomed Eng Online 8:30.

Forouhar AS, Liebling M, Hickerson A, Nasiraei-Moghaddam A, Tsai HJ, Hove JR, Fraser SE, Dickinson ME, Gharib M. 2006. The embryonic vertebrate heart tube is a dynamic suction pump. Science 312:751–753.

Girard PR, Nerem RM. 1993. Endothelial cell signaling and cytoskeletal changes in response to shear stress. Front Med Biol Eng 5:31–36.

Goodwin RL, Nesbitt T, Price RL, Wells JC, Yost MJ, Potts JD. 2005. Three-dimensional model system of valvulogenesis. Dev Dyn 233:122–129.

Groenendijk BC, Hierck BP, Vrolijk J, Baiker M, Pourquie MJ, Gittenberger-de Groot AC, Poelmann RE. 2005. Changes in shear stress-related gene expression after experimentally altered venous return in the chicken embryo. Circ Res 96:1291–1298.

Hierck BP, Van der Heiden K, Poelma C, Westerweel J, Poelmann RE. 2008. Fluid shear stress and inner curvature remodeling of the embryonic heart. choosing the right lane!. Sci World J 8:212–222.

Hogers B, DeRuiter MC, Baasten AM, Gittenberger-de Groot AC, Poelmann RE. 1995. Intracardiac blood flow patterns related to the yolk sac circulation of the chick embryo. Circ Res 76:871–877.

Hove JR, Koster RW, Forouhar AS, Acevedo-Bolton G, Fraser SE, Gharib M. 2003. Intracardiac fluid forces are an essential epigenetic factor for embryonic cardiogenesis. Nature 421:172–177.

Hu N, Clark EB. 1989. Hemodynamics of the stage 12 to stage 29 chick embryo. Circ Res 65:1665–1670.

Hu N, Christensen DA, Agrawal AK, Beaumont C, Clark EB, Hawkins JA. 2009. Dependence of aortic arch morphogenesis on intracardiac blood flow in the left atrial ligated chick embryo. Anat Rec (Hoboken) 292:652–660.

Jaffee OC. 1965. Hemodynamic factors in the development of the chick embryo heart. Anat Rec 151:69–75.

Jenkins MW, Chughtai OQ, Basavanhally AN, Watanabe M, Rollins AM. 2007. In vivo gated 4D imaging of the embryonic heart using optical coherence tomography. J Biomed Opt 12:030505.

Kilner PJ, Yang GZ, Wilkes AJ, Mohiaddin RH, Firmin DN, Yacoub MH. 2000. Asymmetric redirection of flow through the heart. Nature 404:759–761.

Kohl T. 2002. Fetal echocardiography: New grounds to explore during fetal cardiac intervention. Pediatr Cardiol 23:334–346.

Liebling M, Forouhar AS, Wolleschensky R, Zimmermann B, Ankerhold R, Fraser SE, Gharib M, Dickinson ME. 2006. Rapid three-dimensional imaging and analysis of the beating embryonic heart reveals functional changes during development. Dev Dyn 235:2940–2948.

Liu A, Rugonyia S, Pentecostb. J.O., Thornburgb KL. 2007. Finite element modeling of blood flow-induced mechanical forces in the outflow tract of chick embryonic hearts. Comput Struct 85:727–738.

Manning A, McLachian JC. 1990. Looping of chick embryo hearts in vitro. J Anat 168:257–263.

McQuinn TC, Bratoeva M, Dealmeida A, Remond M, Thompson RP, Sedmera D. 2007. High-frequency ultrasonographic imaging of avian cardiovascular development. Dev Dyn 236:3503–3513.

Miller CE, Vanni MA, Taber LA, Keller BB. 1997. Passive stress-strain measurements in the stage-16 and stage-18 embryonic chick heart. J Biomech Eng 119:445–451.

Patten BM, Kramer TC, Barry A. 1948. Valvular action in the embryonic chick heart by localized apposition of endocardial masses. Anat Rec 102:299–311.

Phoon CK, Ji RP, Aristizabal O, Worrad DM, Zhou B, Baldwin HS, Turnbull DH. 2004. Embryonic heart failure in NFATc1-/- mice: novel mechanistic insights from in utero ultrasound biomicroscopy. Circ Res 95:92–99.

Poelma C, Van der Heiden K, Hierck BP, Poelmann RE, Westerweel J. 2010. Measurements of the wall shear stress distribution in the outflow tract of an embryonic chicken heart. J R Soc Interface 7:91–103.

Reckova M, Rosengarten C, deAlmeida A, Stanley CP, Wessels A, Gourdie RG, Thompson RP, Sedmera D. 2003. Hemodynamics is a key epigenetic factor in development of the cardiac conduction system. Circ Res 93:77–85.

Rychter Z, Kopecky M, Lemez L. 1955. A micromethod for determination of the circulating blood volume in chick embryos. Nature 175:1126–1127.

Savard M, Swan HJC, Kirklin JW, Wood EW. 1960. Hemodynamic alterations associated with ventricular septal defects. Congenital Heart Disease. Bass AD, Moe GK, editors. American Association for the Advancement of Science publication number 63.

Sedmera D, Pexieder T, Rychterova V, Hu N, Clark EB. 1999. Remodeling of chick embryonic ventricular myoarchitecture under experimentally changed loading conditions. Anat Rec 254:238–252.

Taber LA, Hu N, Pexieder T, Clark EB, Keller BB. 1993. Residual strain in the ventricle of the stage 16–24 chick embryo. Circ Res 72:455–462.

Tworetzky W, Wilkins-Haug L, Jennings RW, van der Velde ME, Marshall AC, Marx GR, Colan SD, Benson CB, Lock JE, Perry SB. 2004. Balloon dilation of severe aortic stenosis in the fetus: Potential for prevention of hypoplastic left heart syndrome: Candidate selection, technique, and results of successful intervention. Circulation 110:2125–2131.

Usami S, Magazinovic V, Chien S, Gregersen MI. 1970. Viscosity of turkey blood: rheology of nucleated erythrocytes. Microvasc Res 2:489–499.

Vennemann P, Kiger KT, Lindken R, Groenendijk BC, Stekelenburg-de Vos S, ten Hagen TL, Ursem NT, Poelmann RE, Westerweel J, Hierck BP. 2006. In vivo micro particle image velocimetry measurements of blood-plasma in the embryonic avian heart. J Biomech 39: 1191–1200.

Vermot J, Forouhar AS, Liebling M, Wu D, Plummer D, Gharib M, Fraser SE. 2009. Reversing blood flows act through klf2a to ensure normal valvulogenesis in the developing heart. PLoS Biol 7: e1000246.

Wang Y, Dur O, Patrick MJ, Tinney JP, Tobita K, Keller BB, Pekkan K. 2009. Aortic arch morphogenesis and flow modeling in the chick embryo. Ann Biomed Eng 37:1069–1081.

Wilcox DC. 1997. Basic fluid mechanics. La Caftada, CA: DCW Industries, Inc.

Yalcin H, Shekhar A, Rane AA, Butcher JT. 2010. An ex-ovo chicken embryo culture system suitable for imaging and microsurgery applications. J Vis Exp 44, URL: http://www.jove.com/index/Details. stp?ID=2154 [Accessed 30 November 2010].

Yoshida H, Manasek F, Arcilla RA. 1983. Intracardiac flow patterns in early embryonic life. A reexamination. Circ Res 53:363–371.

Developmental Dynamics